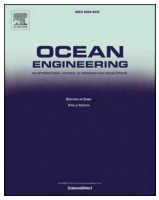
Ocean Engineering 329 (2025) 120797



Contents lists available at ScienceDirect

Ocean Engineering

journal homepage: www.elsevier.com/locate/oceaneng



Research paper



Theoretical model for microbubble drag reduction technique applied to marine propellers

Adelaida García-Magariño *, Suthyvann Sor, Rafael Bardera, Pablo López-Gavilán

Instituto Nacional de Tecnología Aeroespacial "Esteban Terradas" (INTA), Carretera de la Sierra s/n, 28048, Madrid, Spain

ARTICLE INFO

Keywords:
Microbubble drag reduction
Marine propulsion
Theoretical hydrodynamics
Bubbly flow

ABSTRACT

An increase in the propeller efficiency could result in a reduction of the contaminant emissions of ships. The reduction of drag by means of injecting microbubbles in the boundary layer of the blade of propeller is first studied in this article based on the fluid mechanics theory and the fundamental knowledge of this recent technique (that is usually applied to the hull of ships instead). A theoretical approach is proposed to evaluate the drag reduction due to the bubbles presence inside the boundary layer. This is a new application of bubbles dynamic to reduce the drag of the blades of the marine propellers, thus increasing their efficiency.

1. Introduction

The European Maritime Transport Environmental Report, 2021 shows that ships produce 13.5 % of all greenhouse gas emissions from transport in the EU. Since 2013, the International Maritime Organization (IMO) established that every newly built ships must comply with the Energy Efficiency Design Index (EEDI) linked to the type of ship (Kim et al., 2020). A review on the countermeasures for CO_2 emissions from ships can be found in Xing et al. (2020). The main source of gas emission is due to the propulsion systems (Simonsen et al., 2018; Ren et al., 2019) and many studies has been dedicated to improve the ship propeller efficiency such as the ones of Yin et al. (2023), Gao et al. (2023), Nadery et al. (2021) or those of the group of Tadros et al. (Tadros et al., 2021a, 2021b, 2022a, 2022b, 2023) (even in electric propulsion a propeller is needed, Nuchturee et al. 2020). Yin et al. (2023) improved the propeller efficiency by optimum design of the propeller boss cap fins. Gao et al. (2023) tried to improve the controllable-pitch propeller efficiency. Nadery et al. (2021) investigated a new pre-swirl stator. The group of Tadros et al. (Tadros et al., 2021a, 2021b, 2022a, 2022b, 2023) tried to reduce the fuel consumption by optimized designing of propeller series (Tadros et al., 2021a), contra-rotating propeller (Tadros et al., 2022a), or coupled engine-propeller selection (Tadros et al., 2021b) and studying effects such as the propeller cup in cavitation (Tadros et al., 2022b), or hull and propeller roughness (Tadros et al., 2023). In this context, another less studied way to increase the efficiency of a propeller would be the reduction of the friction drag on its blades. According to the review of Kumar et al. (2021), there are several ways to reduce the friction resistance on a surface such as polymer additives, superhydrophobic coatings or air lubrication. Biomimetic sharkskin riblet (Mawignon et al., 2023) and dolphin-inspired transverse wave microgrooves (Zhen et al., 2024) have also been investigated to reduce drag. However, as stated by Vakarelski et al. (2021), the use of hydrophobic coatings in marine propeller could result in an increase of drag such as for speed-boat propeller in which it could result in up to three-time lower speed because of the inhibition of surface piercing and the prevention of the transition to planning mode. In this context, this article is dedicated to study the application of air lubrication, and in particular the microbubble drag reduction (MBDR) technique, to marine propeller. MBDR technique consists on the injection of microbubbles in the boundary layer of a surface thus modifying the friction resistance of the surface (Feng et al., 2020; Wang et al., 2022; Zhao and Zong, 2022; Xia et al., 2023). Among the different kind of air lubrication techniques, MBDR technique has the advantage that the energy needed to inject the air is considerable smaller, which would result in an increase of the net efficiency.

Regarding the fundamental basis of MBDR, a comprehensive study is found in the review of Murai (2014), which reviewed and discussed the basics mechanisms involved for different bubbles sizes and classified them into multiple regions of the parameter space of interest. Since then, MBDR has been widely studied as shown in the most recent review of García-Magariño et al. (2023). According to García-Magariño et al. (2023), which reviewed all the published works in the last decade related to bubble drag reduction, 33% of them were applied to ships. However, all the works related to ships concerned only the application to the ship's

* Corresponding author.
E-mail address: garciamga@inta.es (A. García-Magariño).

https://doi.org/10.1016/j.oceaneng.2025.120797
Received 25 October 2024; Received in revised form 11 February 2025; Accepted 24 February 2025
Available online 7 April 2025
0029-8018/© 2025 The Authors. Published by Elsevier Ltd. This is an open access article under the CC BY-NC-ND license (http://creativecommons.org/licenses/by-nc-nd/4.0/).

hull and none of them considered the possibility of application MBDR to the blades of the propeller. Recently specific reviews dedicated to the application of MBDR technique to ships, such as the one of Sindagi and Vijayakumar (2021) or An et al. (2022) also confirm that it is always applied to the hull. In this context, the present work is dedicated to the application of MBDR to the blades of ships propellers. As far as the authors know, this is the first time that the microbubble drag reduction technique is considered to be applied to propeller in order to reduce the friction resistance on its blades to increase its propeller's efficiency in a journal article. From a fundamental point of view, there appears a pressure gradient on the profile of a blade of a propeller that did not appeared in a flat plate, and that was usually neglected when the hull was considered. A theoretical approach of drag reduction on a profile is proposed in this article and the final expressions obtained are discussed.

Finally, note that the ultimate goal of drag reduction is to achieve a reduction in energy consumption. In this context, firstly, it is known that MBDR technique can reduce viscous stress up to 80% (according to Sindagi and Vijayakumar, 2021) and there is a great variability of studies on the reduction of viscous stresses by applying air lubrication techniques in ship hulls under real conditions. Regarding the method to estimate the effectiveness of air injection techniques under real conditions and the cost-benefit analysis, the work of Kim and Steen (2023) is very interesting. The authors develop a methodology supported by the semi-empirical results obtained in towing tank and cavitation tunnel installations (Ceccio, 2010; Elbing et al., 2008) for flat plate tests, when characterizing the energy savings in a ship under real conditions. The results reveal that the type of technology used to generate bubbles, the air lubrication regime and ship operating factors are of great importance when characterizing the energy savings. Therefore, the application problem is complex and includes a large number of factors such as the geometry of the propeller, its operating conditions and its surface finish, together with the different injection or bubble generation technologies. Currently, the bubble generation in the blades of the propeller poses still a challenge and is out of the scope of this article. In this context, the proposed theoretical model would allow, once the functions considered known in the development have been characterized experimentally for a specific propeller, to qualitatively estimate the regions where they would have the greatest impact, leaving for future work the estimation of the effective savings in its application.

Regarding the organization of this article, first the literature background on the interaction of bubbles and marine propellers is presented. Then, the development of the theoretical approach proposed for the drag reduction of a profile is shown. After, the final expression obtained for drag reduction is discussed and the main conclusions are obtained.

2. Background of the interaction of bubbles and marine propellers

The interaction of bubbles and propeller is studied in the literature mainly in three situations that differs from the MBDR technique mainly in that bubbles are generally outside the boundary layer. First of all, it is known that a bubble layer can result in acoustic interference (Yu-Zhe et al., 2018; Bae et al., 2022). This is the principle for systems known as PRAIRIE (PRopeller AIR Induced Emission) used to prevent the propagation of noise by generating air bubbles clusters near the propeller (Bae et al., 2022). Therefore, there exist studies regarding the acoustic interference of air-bubbles layers with propellers such as the one of Lee et al. (2014). Lee et al. (2014) conducted experiments on a full-scale commercial 8000 TEU container vessel with six-bladed propeller in which a single-nozzle arrangement that distributes air bubbles around the maximum pressure amplitude was used to reduce the noise and vibration of the cavitation, showing reduction of hull's vibration up to 75%. Moreover, there are studies on the bubble size distribution around underwater vehicles and ships such as the ones of Vahaji et al. (2018) and Li et al. (2019). According to Vahaji et al. (2018), in which exhaust gas was discharged into the flow around an underwater vehicle, many small bubbles would be trapped at the aft of the vehicle. Generally, the bubbles are generated outside the propeller and do not address the interaction of microbubbles with the boundary layer of the blades of the propeller, which is the foundation of the microbubble drag reduction systems applied to marine propeller. However, in some case, air was generating through the foil (Reisman et al., 1997). Reisman et al. (1997) injected air in the NACA 0021 and the NACA64A309 foils by ventilation holes to obtain a large reduction of the noise due to cavitation. Nevertheless, they do not study the friction reduction on its surface.

Secondly, the cavitation problem also involves bubbles near a propeller. In this case, the water static pressure comes down to generate steam bubbles, which may implode when pressure rises thus originating blade's erosion, ship's vibrations and noise. The main problem of cavitation is precisely these implosions and the pressure fluctuations originated. One may think that microbubbles could act as cavitation nuclei. However, according to Mørch (2009), gas bubbles cannot act as cavitation nuclei unless somehow stablished. Moreover, there are studies that concludes that air injection can reduce the unsteady pressure fluctuations (Wang et al., 2018) and the cavitation noise (Reisman et al., 1997).

Finally, the MBDR technique applied to the hull of ships leads to a bubbly flow in the wake that interacts with the propellers and limited studies have been conducted to this regard (Kawamura et al., 2007; Li and Yongpeng, 2012; Wu et al., 2020). In these cases, the propeller encounters a bubbly flow outside the boundary layer, which decreases the flow density and could lead to a reduction of the thrust. Kawamura et al. (2007) studied the reduction of propeller efficiency in bubbly flow numerically. However, they used a model that did not include the effect of bubbles on turbulence or the skin friction coefficient. Li and Yongpeng (2012) also performed a numerical study of the effect of bubble layer of propulsion performance and they concluded that for a deep-vee hull form ship, the bubble layer has small effect. Finally, Wu et al. (2020) conducted numerical simulations with and without propeller about the air layer on the lower surface of a large ship model and they concluded that the average of the axial speed at the propeller disk surface would increase with air injection and the average wake fraction decrease.

3. Theoretical model proposed

The main novelty of this work is the possible application of the MBDR technique to propellers within the naval field. The main difference respect to applying MBDR to a flat plate (or a hull) is the pressure gradient on the surface that appears in the blades of a propeller. In relation to the study of viscous effects on marine propeller blades, one of the methodologies commonly used during the initial stages of propeller analysis and engineering design is the coupling of potential flow solvers with plane boundary layer models. A recent work employing such methodology is described by Wu and Kinnas (2025) where a three-dimensional BEM (Boundary Element Method) is coupled with a two-dimensional boundary layer formulation that incorporates coefficients for three-dimensional effects and interactions between the blades. This work extends previous work such as that of Hufford et al. (1994). In both studies the authors rely on the experimental results of Jessup (1989) that studied the boundary layer that develops on DTMB 4119 propellers, concluding that it develops mainly in the stream tube. Therefore, the radial flows and centrifugal forces on the fluid elements are not relevant in conventional propellers, or in other words, the kinematic variables will be negligible in directions normal to the flow domain, so it can be considered plane. For this simplification to be applied to bubbly flows, the force contributions acting on the bubbles normal to the plane domain (centrifugal and buoyancy) must be negligible compared to the remaining forces driving the bubble motion within the boundary layer. A further analysis of this assumption is discussed in Appendix A.

Taking into account the aforementioned considerations, a theoretical model for the viscous effects on a marine conventional propeller is proposed using the blade element theory. This propeller modeling tool is commonly used in the initial stages of design analysis (Benini, 2004).

The methodology is proposed in order to study the effects of the pressure gradient on the viscous stress reduction mechanism individually and explore its applicability on hydrofoils and marine propellers. The blade element theory applied to propellers allows to analyse the problem from the perspective of the stream tubes that pass through the actuator disk that contains it. This avoids the need to establish a radial balance between the different blade sections, which can be analyzed by means of a moving reference frame fixed to each blade section. This approach will be more accurate the more uniform the circulation distribution over the blades, thus losing accuracy at close to the blade tip and propeller hub. On the other hand, since the flow is two-dimensional, secondary flows will be neglected and therefore transverse flows to the blade element will not be considered. Likewise, it ignores other complex phenomena such as flow separation, asymmetries between the blade elements, blade deformations or interactions between them among others.

Therefore a rotating reference system will be considered linked to the axis of rotation of the propeller and non-deformable blade elements. In addition, symmetrical and stationary downstream and upstream conditions will be considered, so that the movement in regions external to the boundary layer is isenthalpic and therefore the rotational stagnation enthalpy remains constant. These conditions are sufficient to consider the problem stationary for a marine propeller operating in a single-phase medium. In the case of a bubbly flows, an additional condition is required since the direction of the gravitational axis is usually normal to the axilsymmetry axis. In particular, buoyancy forces must be negligible when compared to the other forces involved in the bubble motion within the boundary layer. In relation to the former, numerical studies such as those by Mattson and Mahesh (2011) and Zhang et al. (2020), where DNS coupled with Euler-Lagrangian models are used to study the kinematics and interaction of bubble swarms and the turbulent flow developed over a flat plate, have concluded that the lift caused by the shear flow, and in particular the added mass force, are dominant when it comes to dispersing the bubbles further from the wall, being the bouyancy of little relevance in their dispersion.

Taking into account the aforementined consideration, the following assumptions regarding the propeller flow field will be made.

- The propeller is analyzed using the blade element theory, with the simplifications described above. The axial velocity U_a and the rotation speed of the propeller ω are considered constant so that for a distance to the rotation axis r the stream velocity for a given blade cross-section can be described as:

$$\vec{U}_\infty(r) = U_a \vec{i} + \omega r \vec{j}$$

- The Reynolds number for each blade section is described as $Re = U_\infty\, c/\nu_L$, being c the chord of the considered blade section and ν_L the kinematic viscosity of liquid phase.
- The centrifugal force effect on the bubble dispersion is considered negligible (A more comprehensive discussion of this approximation can be found in Appendix A).
- The buoyancy force effect on the bubble motion within boundary layer is also considered negligible (A more comprehensive discussion of this approximation can be found in Appendix A).
- Under these assumptions, the problem becomes periodically axisymmetric and can be considered stationary.
- These assumptions also allows to analyse the viscous effects within a Plane Flow domain.

Therefore, we will depart from describing the properties of the boundary layer through the traditional Von Karman integral equation. Considering Reynolds number, $Re \gg 1$ with perfectly attached flow so there is no separation, the flat fluid domain containing the blade element is divided into two distinct regions, an outer irrotational region characterised by the potential flow solution and an inner infinitesimal region close to the wall with thickness of order $\delta_u \sim O(L_x Re^{-\alpha})$ where viscous effects are included, being L_x a characteristic length, which for the overall blade element surface is described by the chord, c, and for the regions of higher curvature (near the leading edge) can be approximated by its local radius of curvature ($L_x = R_c$). Thus under the boundary layer thickness conditions $\delta_u \ll c \ll R_c$, the curvature terms appearing in the cylindrical Navier-Stokes equations will be negligible with an error of order Re^{-1}. Under this approximation and considering $Re \gg 1$, the boundary layer equations can be expressed in local Cartesian coordinates. A first order asymptotic expansion of the full solution for the inner region will therefore be used. A more extensive description of this fluid domain description can be found in Leal (2007). Therefore, under the hypotheses considered, the effect of the curvature in the inner region is taking into account only through the pressure gradient, so the velocity outside the boundary layer varies as $U_e(x)$, where x is the tangential component to the surface and y is the normal component, as shown in Fig. 1. It will also be assumed that the density of the mixture of the gaseous phase, in the form of bubbles, and the liquid phase can be expressed as a continuous medium with density $\rho(x,y)$, which will vary in a region of the boundary layer with thickness $\delta_\rho(x)$, until reaching a constant density equal to that of the liquid phase ρ_e. We will also define the thickness of the boundary layer through the variable $\delta_u(x)$, its value always being greater than or equal to $\delta_\rho(x)$ for the same x. Note that by assuming a continuous medium, buoyancy of the bubbles are not considered and therefore this theory could only be applied to the cases where buoyancy of the bubbles can be neglected, which in practical situations corresponds to the cases of high Reynodls number (see Appendix A), which is one of the considerations assumed.

First of all, we depart from the traditional hypotheses for boundary layers, which follows.

- The flow is slender such that the characteristic length in the longitudinal direction L_x is much larger than the boundary layer thickness.

$$L_x \gg \delta_u \tag{1}$$

- In this way, since this thickness of the boundary layer $\delta_u \ll c \ll R_c$, the curvature terms that appear in the Navier-Stokes equations in cylindrical coordinates will be negligible, as discussed before, and the boundary layer equations can be expressed in local Cartesian coordinates.
- The pressure inside the boundary layer is assumed to vary only with the longitudinal direction.

$$\left\{\frac{\partial p}{\partial y} \cong 0 \quad \Rightarrow \quad \frac{\partial p}{\partial x} = \left.\frac{dp}{dx}\right|_{y=\delta_u(x)}\right. \tag{2}$$

- The boundary conditions are:

$$\begin{cases} u(x,\delta_u) = U_e(x) \\ v(x,\delta_u) = V_e(x) \end{cases} \quad \begin{cases} u(x,0) = 0 \\ v(x,0) = 0 \end{cases} \quad \left\{\left.\frac{\partial p}{\partial x}\right|_{y=\delta_u(x)} = \frac{dp_e}{dx}\right. \tag{3}$$

where U_e and V_e are the components of the velocity and p_e is the pressure, obtained from the flow field outside the boundary layer. Note that in the case of screw propeller blades, there exist a pressure gradient due, among others, to the curvature of the blade surface.

Assuming the previous hypotheses, the continuity and momentum equations for the stationary compressible boundary layer are:

$$\frac{\partial(\rho u)}{\partial x} + \frac{\partial(\rho v)}{\partial y} = 0 \tag{4}$$

$$\frac{\partial(\rho u^2)}{\partial x} + \frac{\partial(\rho u v)}{\partial y} + \frac{dp_e}{dx} - \frac{\partial \tau_{xy}}{\partial y} = 0 \tag{5}$$

being p_e the pressure outside the boundary layer and τ_{xy} a component of the shear stress tensor $\overline{\overline{\tau}}$.

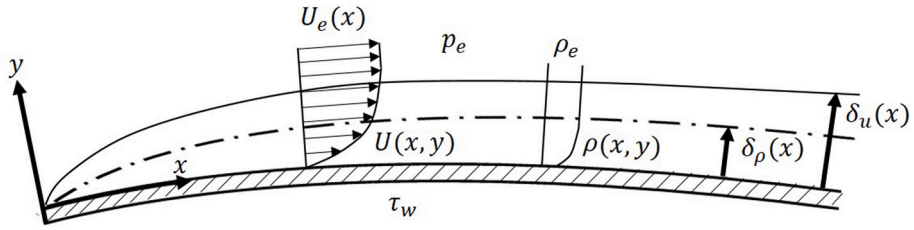


Fig. 1. Boundary layer sketch.

From an analysis of the orders of magnitude of the continuity equation, $\frac{V_e}{U_e} \sim \frac{\delta_u}{L_x}$ and since we have assumed that the flow is slender $\left(\frac{\delta_u}{L_x} \ll 1\right)$, therefore $V_e \ll U_e$. Considering the first order asymptotic expansion of the full solution in the inner region, the y component can be rescaled as $Y = Re^{\alpha}y$, being α an experimental coefficient on the order of the unity. According to the continuity equation, the magnitude of the velocities on the local Cartesian scale x,Y must depend on the Re number. At the asymptotic limit between the outer and inner region, the tangential velocity $u(x,\delta_u)/U_e \to 1$, and the normal component $v(x,\delta_u)/U_e$ will be of order $O(Re^{-\alpha})$. Integrating both equations along the boundary layer we obtain:

$$\int_0^{\delta_u(x)} \frac{\partial(\rho u)}{\partial x} dy + \int_0^{\delta_u(x)} \frac{\partial(\rho v)}{\partial y} dy = 0 \tag{6}$$

$$\int_0^{\delta_u(x)} \frac{\partial(\rho u^2)}{\partial x} dy + \rho_e U_e V_e + \frac{dp_e}{dx}\delta_u + \tau_{xy}\big|_{y=0} = 0 \tag{7}$$

where V_e is the normal direction component of the velocity in $y = \delta_u(x)$. Using Liebniz's rule it is possible to transform the partial derivatives into total ones:

$$\frac{d}{dx}\int_0^{\delta_u(x)} \rho u dy = \int_0^{\delta_u(x)} \frac{\partial(\rho u)}{\partial x} dy + \rho_e U_e \frac{d\delta_u}{dx} \tag{8}$$

$$\frac{d}{dx}\int_0^{\delta_u(x)} \rho u^2 dy = \int_0^{\delta_u(x)} \frac{\partial(\rho u^2)}{\partial x} dy + \rho_e U_e^2 \frac{d\delta_u}{dx} \tag{9}$$

By substituting (9) in (7), we obtain:

$$\frac{d}{dx}\int_0^{\delta_u(x)} \rho u^2 dy - \rho_e U_e^2 \frac{d\delta_u}{dx} + \rho_e U_e V_e + \frac{dp_e}{dx}\delta_u + \tau_{xy}\big|_{y=0} = 0 \tag{10}$$

and proceeding to substitute (8) in (6) and multiplying by $U_e(x)$, we also obtain:

$$\frac{dU_e}{dx}\int_0^{\delta_u(x)} \rho u dy - \frac{d}{dx}\int_0^{\delta_u(x)} \rho u U_e dy = \rho_e U_e V_e - \rho_e U_e^2 \frac{d\delta_u}{dx} \tag{11}$$

which replaced in (10) would result in:

$$\frac{d}{dx}\int_0^{\delta_u(x)} (\rho u^2 - \rho u U_e) dy + \frac{dU_e}{dx}\int_0^{\delta_u(x)} \rho u dy + \frac{dp_e}{dx}\delta_u = -\tau_w \tag{12}$$

Now, let us consider the following identities:

$$\frac{dU_e}{dx}\int_0^{\delta_u(x)} \rho_e U_e dy - \rho_e U_e \frac{dU_e}{dx}\delta_u = 0 \tag{13}$$

$$\frac{dp_e}{dx}\delta_u + \rho_e U_e \frac{dU_e}{dx}\delta_u = 0 \tag{14}$$

By subtracting (13) and (14) both from (12), we arrive at the Von Karman integral momentum equation for compressible boundary layers,

$$\frac{d}{dx}\int_0^{\delta_u(x)} (\rho u^2 - \rho u U_e) dy + \frac{dU_e}{dx}\int_0^{\delta_u(x)} (\rho u - \rho_e U_e) dy = -\tau_w \tag{15}$$

Note that if we considered $\rho(x,y) = \rho_e$, which is equivalent to the case without a gas phase, this equation would take the form of an incompressible boundary layer taking the following form based on its integral relations:

$$\tau_{w_0} = \frac{d}{dx}(\rho_e U_e^2 \theta) + \rho_e U_e \delta^* \frac{dU_e}{dx} \tag{16}$$

being θ the momentum thickness and δ^* the displacement thickness which would be expressed as:

$$\delta^* = \int_0^{\delta(x)} \left(1 - \frac{u}{U_e}\right) dy \tag{17}$$

$$\theta = \int_0^{\delta(x)} \frac{u}{U_e}\left(1 - \frac{u}{U_e}\right) dy \tag{18}$$

where $\delta(x)$ is the boundary layer thickness.

Now, we will assume the following hypotheses in order to be able to model the drag reduction.

- In analogy with the flat plate boundary layer problem we will assume that the velocity inside the boundary layer $u(x,y)$ is a self-similar quantity scaled with $U_e(x)$, defined through the variable $\eta = y/\delta(x)$ by the following power-law dependency:

$$\frac{u(x,y)}{U_e(x)} = \eta^n \tag{19}$$

  where n is a semi-empirical fit exponent.
- The density $\rho(x,y)$ can be expressed from a self-similar quantity when it is scaled through the density deficit, $\rho_s(x) = \rho_e - \rho_w(x)$, such that the following function, $g(\xi)$, is defined as monotonous:

$$g(\xi) = \frac{\rho_e - \rho(x,y)}{\rho_e - \rho_w(x)} \tag{20}$$

  being $\xi = y/\delta_\rho(x)$ and $\rho_w(x) = \rho(x,0)$. In this way, the density can be expressed as:

$$\rho(x,y) = \rho_e - (\rho_e - \rho_w) g(\xi) \tag{21}$$

On the other hand, given the characteristic lengths of the problem, $\partial\xi/\partial x \ll \partial\xi/\partial y$ and $\partial\eta/\partial x \ll \partial\eta/\partial y$, it is possible to relate both dimensionless variables and their derivatives as:

$$\eta = \frac{\delta_\rho}{\delta_u}\xi = k_\delta \xi \tag{22}$$

$$dy \cong \delta_\rho d\xi \cong \delta_u d\eta \tag{23}$$

Under these hypotheses it is possible to replace the definition of density (21) in (15) and it is possible to group the terms as follows:

$$-\frac{d}{dx}\int_0^{\delta_u(x)}(\rho_e u^2-\rho_e u U_e)dy-\frac{dU_e}{dx}\int_0^{\delta_u(x)}(\rho_e u-\rho_e U_e)dy$$
$$+\frac{d}{dx}\int_0^{\delta_u(x)}(\rho_e-\rho_w)g(\xi)(u^2-uU_e)dy+\frac{dU_e}{dx}\int_0^{\delta_u(x)}(\rho_e-\rho_w)g(\xi)udy=\tau_w \tag{24}$$

The two terms on the left can be replaced by the viscous stress tensor for the single-phase case (defined in Eq. (16)), assuming that the integrals terms (as defined in Eqs. (17) and (18)) are the same as in the monophasic case. Therefore:

$$\tau_w-\tau_{w_0}=\frac{d}{dx}\int_0^{\delta_u(x)}(\rho_e-\rho_w)g(\xi)(u^2-uU_e)dy+\frac{dU_e}{dx}\int_0^{\delta_u(x)}(\rho_e-\rho_w)g(\xi)udy \tag{25}$$

The void fraction near the wall ($y=0$) can be expressed as $\alpha_w=1-\rho_w/\rho_e$ being a function that depends only of x. By replacing it and defining the reduction of viscous stress as $DR=1-\tau_w/\tau_{w_0}$, the previous equation takes the form:

$$DR=\frac{\rho_e}{\tau_{w_0}}\left(\frac{d}{dx}\int_0^{\delta_u(x)}\alpha_w(x)g(\xi)(uU_e-u^2)dy-\frac{dU_e}{dx}\int_0^{\delta_u(x)}\alpha_w(x)g(\xi)udy\right) \tag{26}$$

In view of the integration based on the self-similarity hypothesis for the velocity profile in the boundary layer, we can express (26) as follows:

$$DR=\frac{\rho_e}{\tau_{w_0}}\left[\frac{d}{dx}\left(\alpha_w U_e^2\int_0^{\delta_u(x)}g(\xi)\eta^n(1-\eta^n)dy\right)-\alpha_w U_e\frac{dU_e}{dx}\int_0^{\delta_u(x)}g(\xi)\eta^n dy\right] \tag{27}$$

Now, we derive the product of the first term on the right to group the terms that depend on the pressure gradient, leading to the following expression:

$$DR=\frac{\rho_e U_e}{\tau_{w_0}}\left[U_e\frac{d}{dx}\left(\alpha_w\int_0^{\delta_u(x)}g(\xi)\eta^n(1-\eta^n)dy\right)+\alpha_w\frac{dU_e}{dx}\int_0^{\delta_u(x)}g(\xi)(\eta^n(1-\eta^n)-\eta^{2n})dy\right] \tag{28}$$

Taking into account that $g(\xi)=0$ for $\xi>1$, changing the variable y to η and applying the mean value theorem, we found that there exist $C_1=\overline{g(\xi)_1}$ and $C_2=\overline{g(\xi)_2/C_1}$ such that:

$$\int_0^{\delta_u(x)}g(\xi)\eta^n(1-\eta^n)dy=\int_0^{\delta_\rho(x)}g(\xi)\eta^n(1-\eta^n)dy=\overline{g(\xi)_1}\,\delta_u(x)\int_0^{k_\delta}\eta^n(1-\eta^n)d\eta$$
$$=C_1\,\delta_u(x)k_\delta^{n+1}\left(\frac{1}{n+1}-\frac{k_\delta^n}{2n+1}\right) \tag{29}$$

$$\int_0^{\delta_u(x)}-g(\xi)\eta^{2n}dy=-\overline{g(\xi)_2}\,\delta_u(x)k_\delta^{n+1}\frac{k_\delta^n}{2n+1}=-C_1\delta_u(x)k_\delta^{n+1}\frac{C_2k_\delta^n}{2n+1} \tag{30}$$

Substituting (29) and (30) in (28) and deriving the product of the first term on the right with respect to x we have:

$$DR=\frac{\rho_e U_e C_1}{\tau_{w_0}}\left[U_e\alpha_w\left(\delta_u\frac{dH_1}{dx}+H_1\frac{d\delta_u}{dx}\right)+U_e\delta_u H_1\frac{d\alpha_w}{dx}+\alpha_w\delta_u\frac{dU_e}{dx}(H_1-C_2H_2)\right] \tag{31}$$

where

$$H_1(x)=k_\delta^{n+1}\left(\frac{1}{n+1}-\frac{k_\delta^n}{2n+1}\right) \tag{32}$$

$$H_2(x)=k_\delta^{n+1}\frac{k_\delta^n}{2n+1} \tag{33}$$

Fig. 2 shows H_1 and H_2. Note that H_1 is always positive since k_δ is always less than or equal to 1.

Now, defining the skin friction coefficient for the monophasic case as $c_{f0}=2\tau_{w_0}/\rho_e U_\infty^2$ and the new function $H_3=H_1-C_2H_2$, and using the chord of the airfoil c and the upstream unperturbed velocity U_∞ as the characteristic length and velocity respectively, then equation (31) can be expressed as a function of dimensionless variables such as $\overline{U_e}=\frac{U_e}{U_\infty}$, $\overline{\delta_u}=\frac{\delta_u}{c}$ or $\zeta=x/c$, among others:

$$DR=\frac{2C_1}{c_{f0}}\left[\overline{U_e}^2\left(\overline{\delta_u}\frac{dH_1}{d\zeta}+H_1\frac{d\overline{\delta_u}}{d\zeta}\right)\alpha_w+\overline{U_e}^2\overline{\delta_u}H_1\frac{d\alpha_w}{d\zeta}+\overline{\delta_u}H_3\overline{U_e}\frac{d\overline{U_e}}{d\zeta}\alpha_w\right] \tag{34}$$

Equation (34) can be summarized as follows:

$$DR=g_0\left[\left(g_1\overline{U_e}^2+g_2\overline{U_e}\frac{d\overline{U_e}}{d\zeta}\right)\alpha_w+g_3\overline{U_e}^2\frac{d\alpha_w}{d\zeta}\right] \tag{35}$$

Where

$$\begin{cases}g_0(\zeta)=\dfrac{2C_1}{c_{f0}(\zeta)}\\ g_1(\zeta)=\left(\overline{\delta_u}(\zeta)\dfrac{dH_1(k_\delta(\zeta),n)}{d\zeta}+H_1(k_\delta(\zeta),n)\dfrac{d\overline{\delta_u}(\zeta)}{d\zeta}\right)\\ g_2(\zeta)=\overline{\delta_u}(\zeta)H_3(k_\delta(\zeta),n,C_2)\\ g_3(\zeta)=\overline{\delta_u}(\zeta)H_1(k_\delta(\zeta),n)\end{cases} \tag{36}$$

Note that in the end the drag reduction depends on the density variation (through the proportion of the boundary layer filled with bubbles k_δ, the void fraction at the wall α_w and its derivative respect to the longitudinal direction $\frac{d\alpha_w}{d\zeta}$ and the constants C_1 and C_2 that depends on the shape of the self-similarity function for the density), the structure of the boundary layer (through the thickness of the boundary layer δ_u and the exponent of the power-law used for the velocity boundary layer n), and the pressure distribution outside the boundary layer (through $\overline{U_e}^2$ and $\overline{U_e}\frac{d\overline{U_e}}{d\zeta}$ functions that, assuming an infinitely thin boundary layer and therefore a constant total pressure along the streamline in the outer boundary layer limit, can be expressed as $\overline{U_e}^2=1-c_p$ and $\overline{U_e}\frac{d\overline{U_e}}{d\zeta}=-\frac{1}{2}\frac{dc_p}{d\zeta}$ where c_p is the pressure coefficient defined as $c_p=\frac{p-p_e}{\frac{1}{2}\rho_e U_e^2}$).

As indicated by Murai (2014), there is a wide parameter space, with complex non-linear multivariable functions. Generally, the variable of interest is the one considered in this work, the viscous stresses on the wall (τ_w), with three base parameters that directly affect it, which are the volumetric flow rate of the gas phase (Q_b), the external flow velocity (U_e) and the average bubble size (d_b). In general, the parameter space collects parameters linked to the specific conditions of the flow in the external region (pressure gradients, stagnation points, static pressure), the internal conditions of the boundary layer (boundary layer thickness, velocity distribution inside), bubble generation conditions (volumetric flow rate of the gas phase, bubble generation/injection area, surface wettability), and properties of the bubble swarm (Weber number, Bond number, relative size between bubbles and boundary layer, Froude

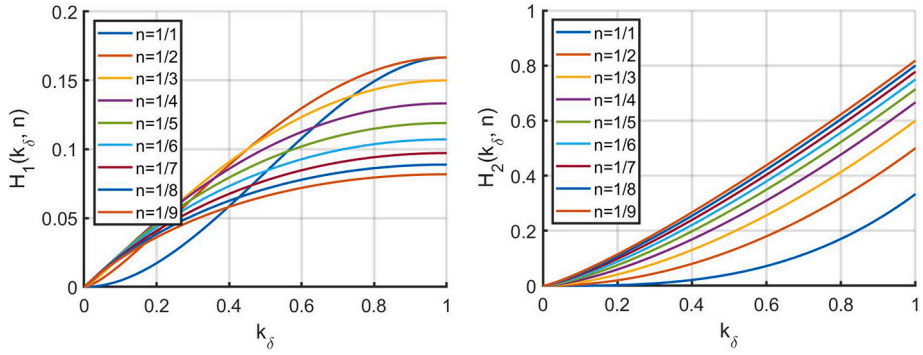


Fig. 2. Functions H_1 and H_2.

number, interactions between bubbles). In the context of the hypotheses assumed, this wide parameter space have been collected through the proposed variables (α_w, $\frac{d\alpha_w}{dx}$, $g(\xi)$, k_δ, U_e, $\frac{dU_e}{dx}$, δ_u, $\frac{d\delta_u}{dx}$) thus presenting the advantage that they are magnitudes that are reasonably measurable from the experimental point of view.

Finally, the monotonic function for the void fraction could be discussed. Although the monotonic function hypothesis for the void fraction is a simplification used in models such as the one described in Park et al. (2016), the physical foundation is still under study and has been normally adopted on the basis of experimental observations referring to the time averages for MBDR and BDR tests (Gabillet et al. (2002), Sanders et al. (2006) and Park et al. (2023) among others), where some authors highlight the difficulty of taking measurements of the void fraction in regions close to the wall. These experimental observations on the other hand are highly influenced by the way in which the bubbles are generated and the flow conditions in which they disperse. And, as indicated by Mattson and Mahesh (2011), "… the mechanisms of bubble dispersion away from the wall has not been well understood …". On the other hand, the volume fraction close to the wall is one of the variables with the greatest impact on the mechanism of viscous stress reduction (Guin et al., 1996). Nevertheless, numerical simulations for cases of bubbles injected in a flat plate turbulent boundary layer (Mattson and Mahesh, 2011; Zhang et al., 2020) or the LES numerical study by Feng et al. (2020) have shown that the maximum void fraction is located in regions close to the wall ($y^+ < 15$) and then decreases to zero when it moves away from it. However, in the work of Mattson and Mahesh (2011) for bubbles injected at a single point and with sizes at the injection point $R_b < 10^{-2}\ \delta_u$, an interesting conclusion is reached and that is that the behavior observed by the bubbles and that of the passive scalars is qualitatively very similar, collapsing the bubble concentrations when they are scaled with the local maximum concentration and with the thickness of the local bubble layer. We have used these observations as a first approximation when constructing the model hypotheses such that the void fraction distribution function will behave monotonically decreasing and will present a self-similarity in local coordinates x. It should be noted that this hypothesis must be evaluated experimentally in the context of pressure gradients to characterize the function $g(\xi)$, and the different length scales involved in its normalization.

4. Results and discussions

In the previous section we have obtained a final expression (Eq. (35)) for the drag reduction that depends on four functions: $g_0(\zeta)$, $g_1(\zeta)$, $g_2(\zeta)$ and $g_3(\zeta)$. In order to study the different contributions to the drag reduction, the drag reduction has been divided into the following three terms to study separately the contribution of each term:

$$DR = \Delta(DR)_1 + \Delta(DR)_2 + \Delta(DR)_3 \tag{37}$$

Where

$$\begin{cases} \Delta(DR)_1 = g_0 g_1 \overline{U_e}^2 \alpha_w \\ \Delta(DR)_2 = g_0 g_2 \overline{U_e} \dfrac{d\overline{U_e}}{d\zeta} \alpha_w \\ \Delta(DR)_3 = g_0 g_3 \overline{U_e}^2 \dfrac{d\alpha_w}{d\zeta} \end{cases} \tag{38}$$

In the next subsection, each of the drag contribution terms will be studied and discussed. Note that $DR > 0$ would mean that there is a drag reduction, while if it were negative ($DR < 0$), it would mean that there is an increase in drag instead of a reduction.

4.1. Contribution of the pressure gradient to the drag reduction

As explained in the introduction, in the blades of the marine propellers there appears a pressure gradient on the surface and therefore, a new drag reduction term has appeared as compared with previous investigations. This new term, that is the one that contains the function $g_2(\zeta)$, follows:

$$\Delta(DR)_2 = g_0 g_2 \overline{U_e} \frac{d\overline{U_e}}{d\zeta} \alpha_w = -\frac{C_1}{c_{f0}} \overline{\delta_u} H_3 \frac{dc_p}{d\zeta} \alpha_w \tag{39}$$

where

$$H_3 = k_\delta^{n+1} \left(\frac{1}{n+1} - \frac{(1+C_2)k_\delta^n}{2n+1} \right) \tag{40}$$

In order to obtain a drag reduction by this term, it is necessary that $\Delta(DR)_2 > 0$. The sign of C_1, c_{f0}, $\overline{\delta_u}$ and α_w are always positive, while H_3 and $\frac{dc_p}{d\zeta}$ could be positive or negative. Generally, in an airfoil, for the suction face, the function c_p decreases up to a point ζ_c at which it start to increase (note that c_p is negative). For the region where $\frac{dc_p}{d\zeta} > 0$, H_3 should be negative in order to reduce the drag. By examining Eq. (40), H_3 would be negative if only if the following conditions is true:

$$C_2 > \frac{2n+1}{k_\delta^n (n+1)} - 1 \tag{41}$$

In the cases where the bubbles occupy all the boundary layer ($k_\delta = 1$), the function H_3 is negative if only if $C_2 > \frac{n}{n+1}$. Fig. 3 shows the region of the parametric space (C_2, k_δ) where $H_3 > 0$ (in blue) and $H_3 < 0$ (in orange) for different values of n.

If the density function $g(\eta)$ were known, the constants C_1 and C_2 could be calculated as follows:

$$\begin{aligned} C_1 &= \frac{\int_0^{k_\delta} g(\eta)(\eta^n - \eta^{2n}) d\eta}{k_\delta^{n+1} \left(\dfrac{1}{n+1} - \dfrac{k_\delta^n}{2n+1} \right)} \\ C_2 &= \left[\frac{2n+1}{k_\delta^n (n+1)} - 1 \right] \frac{\int_0^{k_\delta} g(\eta) \eta^{2n} d\eta}{\int_0^{k_\delta} g(\eta)(\eta^n - \eta^{2n}) d\eta} \end{aligned} \tag{42}$$

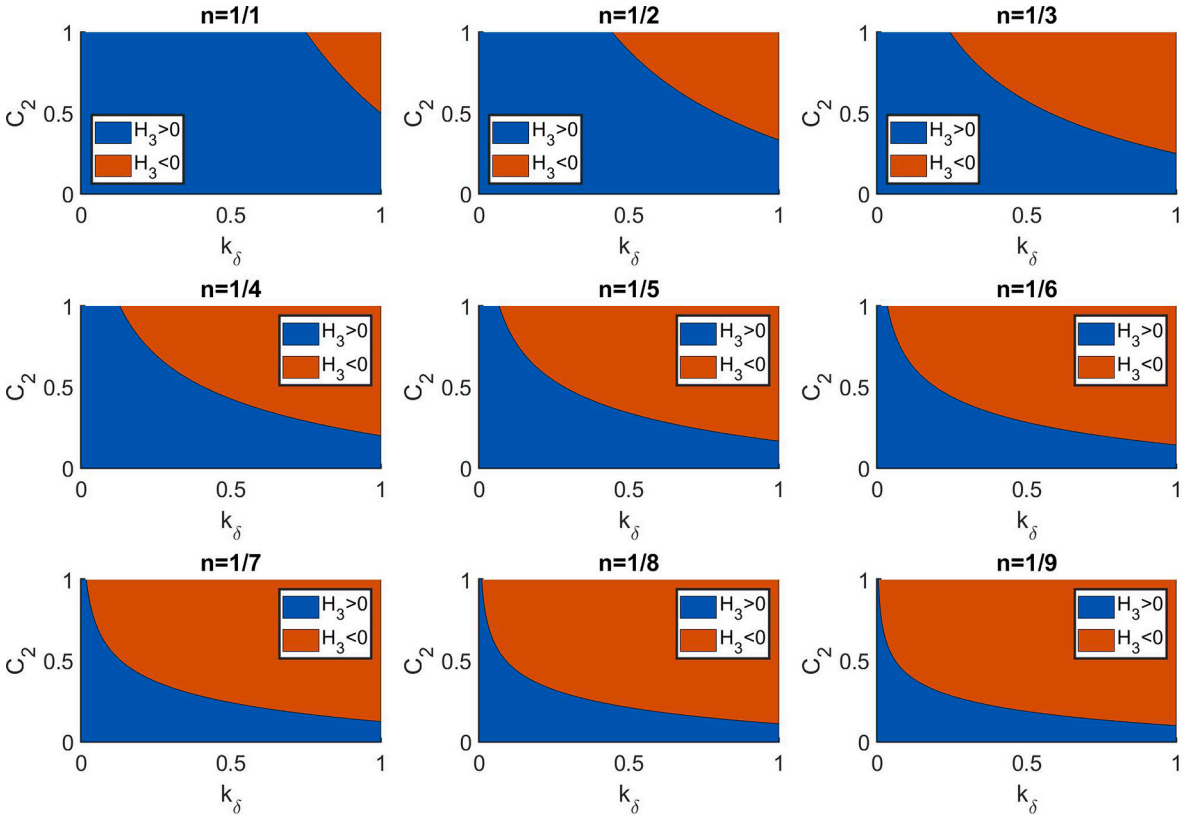


Fig. 3. Maps of the sign of the function H_3 for different k_δ, C_2 and n where blue stands for positive values and orange for negative values.

Therefore, we are going to study what would happen for two different density functions. In particular we are going to study the cases of linear density function and quadratic density function. Table 1 define these functions and shows the calculated C_1 and C_2 with equation (42), that depends on the values of k_δ and n as shown in Fig. 4.

For the sake of clarity, the relation between C_2 and k_δ, obtained from Eq. (41), for each value of n is plotted over Fig. 3 so as to be able to determine for each value of k_δ and n if H_3 is positive or negative. Fig. 5 shows the results. For a general case, it can also be observed in Fig. 5 that as long as a minimum value of k_δ is reached, there is a drag reduction for the region where $\frac{dc_p}{d\zeta} > 0$.

For each k_δ, C_2 would be larger than $\frac{2n+1}{k_\delta^n(n+1)} - 1$ (and therefore H_3 negative) if only if n is below a critical value n_{crit}. Fig. 6 shows these critical values for each density function considered in Table 1. In this figure, the classical value of $n = 1/7$ of the solution of Prandlt is also displayed for comparison purpose.

For the density functions considered and a given k_δ, as long as n is less than a critical value n_{crit}, H_3 would be negative and this term would contribute to reduce drag as long as $\frac{dc_p}{d\zeta} > 0$. In the case that the bubbles occupy all the boundary layer ($k_\delta = 1$), the value n_{crit} is in both cases larger than or equal to the unity, and consequently, it can be inferred that the bubble injection in the airfoil should occupy the region in which the pressure coefficient increases: $\frac{dc_p}{d\zeta} > 0$. From another point of view, Fig. 6 also represents the minimum value of the relative bubble layer thickness relative to the boundary layer thickness, $k_{\delta crit}$, above which, for a given value of the exponent n, H_3 becomes negative. For example, considering the case of a power law with exponent $n = 1/7$, equivalent to that of the Prandtl boundary layer, the critical thicknesses would be $k_{\delta crit} = 0.0246$ for the density function defined by the expression $g(\eta) = 1 - \eta/k_\delta$ and $k_{\delta crit} = 0.0282$ for the density function $g(\eta) = 1 - \eta^2/k_\delta^2$. On the other hand, assuming a boundary layer described by the power law $n = 1/5$, the values would be $k_{\delta crit} = 0.0915$ and $k_{\delta crit} = 0.1044$ for the density functions $g(\eta) = 1 - \eta/k_\delta$ and $g(\eta) = 1 - \eta^2/k_\delta^2$ respectively. From these results, it can be deduced that, as a consequence of the definition of C_2 from Eq. (41), where a quotient of definite integrals is found, the difference between the values of critical thicknesses for the considered density functions is larger the larger the value of the exponent n, being its relative difference in any case less than 19% for $n \leq 1$. Thus, the larger the value of k_δ or the larger the exponent n of the boundary layer, the more relevant it is to describe the density function accurately in order to characterize precisely the point at which H_3 changes the sign.

Finally, Fig. 7 shows the value of H_3 versus k_δ for each density function considered and for each value of n, where the minimum of k_δ

Table 1
Density function.

$g(\eta)$	C_1	C_2
$\begin{cases} 0 & \forall \eta > k_\delta \\ 1 - \frac{\eta}{k_\delta} & \forall \eta \in [0, k_\delta] \end{cases}$	$\frac{(2n+1)(2n+2) - k_\delta^n(n+1)(n+2)}{(n+2)(2n+2)\left[(2n+1) - k_\delta^n(n+1)\right]}$	$\frac{(n+2)\left[(2n+1) - k_\delta^n(n+1)\right]}{(2n+2)(2n+1) - k_\delta^n(n+2)(n+1)}$
$\begin{cases} 0 & \forall \eta > k_\delta \\ 1 - \frac{\eta^2}{k_\delta^2} & \forall \eta \in [0, k_\delta] \end{cases}$	$\frac{2\left[(2n+1)(2n+3) - k_\delta^n(n+1)(n+3)\right]}{(n+3)(2n+3)\left[(2n+1) - k_\delta^n(n+1)\right]}$	$\frac{(n+3)\left[(2n+1) - k_\delta^n(n+1)\right]}{(2n+3)(2n+1) - k_\delta^n(n+3)(n+1)}$

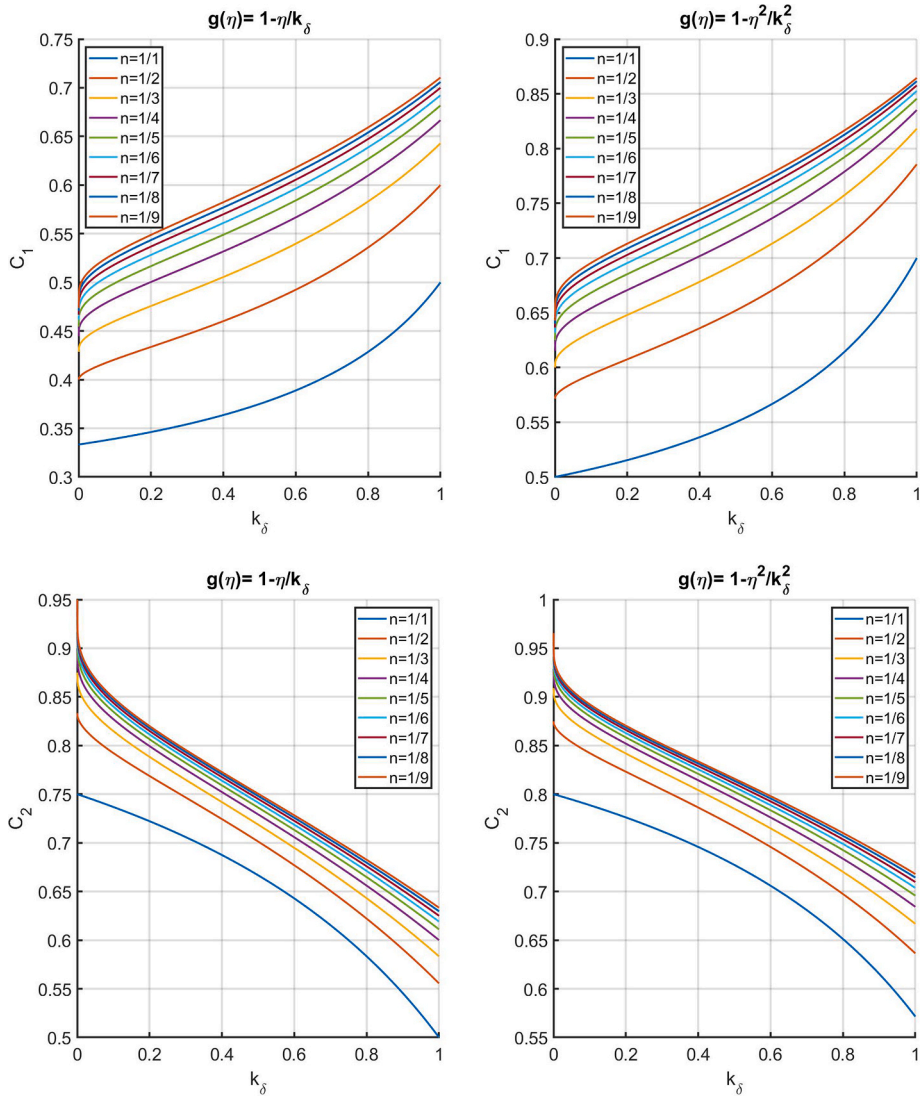


Fig. 4. C_1 and C_2 for linear and quadratic density functions.

can be obtained. One of the conclusions that can be drawn from this figure is that for each curve (with the corresponding value of n), there exists a value $k_{\delta opt} < k_{\delta crit}$ for which H_3 is maximum (and positive). This allows to determine for a boundary layer structure defined from the exponent n, the optimal bubble layer configuration for regions where $\frac{dc_p}{d\zeta} < 0$. On the other hand it is noticeable that for the same value of the pressure gradient, sufficiently low values of exponent n yield negligible maximum values H_3 ($k_{\delta opt}$) when compared to those H_3 values found for $k_\delta \sim O(1)$. Thus for instance we find that for the studied density functions, the boundary layer described by Prandtl's boundary layer exponent ($n = 1/7$) shows maximum values $H_3(k_{\delta opt}) = 0.0013$ being $k_{\delta opt} = 0.011$ for $g(\eta) = 1 - \eta/k_\delta$ and $H_3(k_{\delta opt}) = 0.0011$ being $k_{\delta opt} = 0.009$ for $g(\eta) = 1 - \eta^2/k_\delta^2$. For such boundary layer conditions, in those hydrofoil regions where $\frac{dc_p}{d\zeta} < 0$ the gas phase supply within the bubble layer should be limited, and may even be disregarded given its low impact on the reduction of viscous stresses on $\Delta(DR)_2$. On the contrary, for those regions where $\frac{dc_p}{d\zeta} > 0$ the gas phase supply should be maximized since, within the limits of the proposed model, H_3 has a larger value (at $k_\delta = 1$ $H_3 = -0.45$ for $g(\eta) = 1 - \eta/k_\delta$ and $H_3 = -0.52$ for $g(\eta) = 1 - \eta^2/k_\delta^2$). However, if we consider the boundary layer case with exponent $n = 1/2$, we find a positive maximum value of $H_3(k_{\delta opt}) = 0.085$ being $k_{\delta opt} = 0.269$ for $g(\eta) = 1 - \eta/k_\delta$ and $H_3(k_{\delta opt}) = 0.080$ being $k_{\delta opt} = 0.248$ for $g(\eta) = 1 - \eta^2/k_\delta^2$. Under these conditions, the $\Delta(DR)_2$ term would exhibit a significant viscous stress reduction in those regions where $\frac{dc_p}{d\zeta} < 0$, with absolute values of H_3 comparable to those obtained for $k_\delta \sim 1$ for the proposed density functions ($H_3 = -0.17$ for $g(\eta) = 1 - \eta/k_\delta$ and $H_3 = -0.22$ for $g(\eta) = 1 - \eta^2/k_\delta^2$). In this case, in order to reduce the bubble layer thickness and therefore the contribution of the gas phase, it could be interesting to supply bubbles in regions where $\frac{dc_p}{d\zeta} < 0$. In any case, both the boundary layer structure and the gas phase distribution function should be characterized.

4.2. Contribution of the void fraction gradient to the drag reduction

The way to introduce/produce bubbles inside the boundary layer is also critical to the effectiveness of this technique, since it will affect the distribution of void fraction along the boundary layer. To this regard, it has appeared a drag reduction term in relation to the void fraction gradient along the chord direction in Eq. (37). This term follows:

$$\Delta(DR)_3 = g_0 g_3 \overline{U_e}^2 \frac{d\alpha_w}{d\zeta} = \frac{2C_1}{c_{f0}} \overline{\delta_u} H_1 (1 - c_p) \frac{d\alpha_w}{d\zeta} \tag{43}$$

In order to obtain a drag reduction by this term, it is necessary that

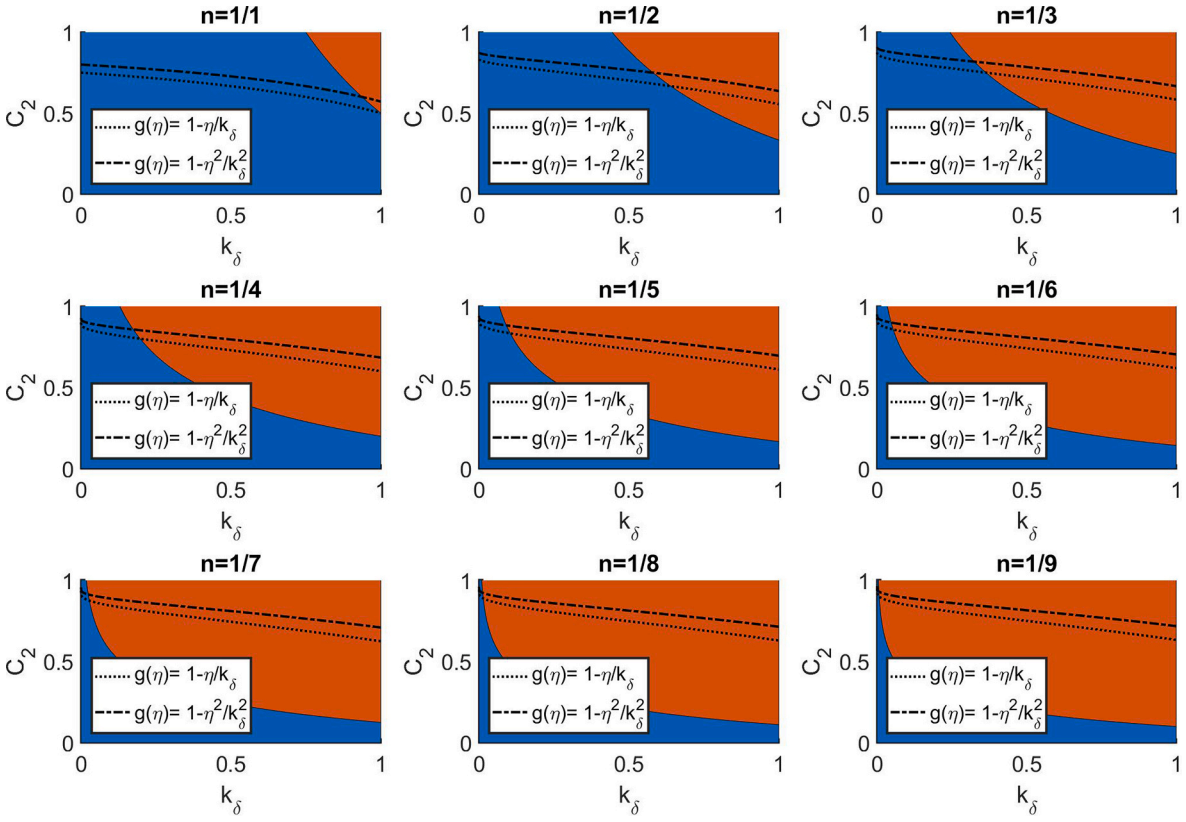


Fig. 5. Maps of the sign of the function H_3 (blue for positive values and orange for negative values).

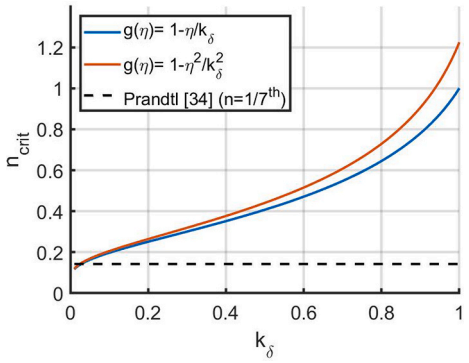


Fig. 6. n_{crit} for linear and quadratic density functions.

$\Delta(DR)_3 > 0$. The sign of C_1, c_{f0}, $\overline{\delta_u}$ and H_1 are always positive, while $\frac{d\alpha_w}{d\zeta}$ could be positive or negative. Therefore, in order to reduce the drag by this term, it is necessary that $\frac{d\alpha_w}{d\zeta} > 0$. Otherwise, this term will contribute to increase drag instead of decrease drag. It is worth mentioning the difference of this term with respect to the traditionally studied case of the flat plate running parallel to the stream as a consequence of the existence of the $(1-c_p)$ term. Considering similar the boundary layer ($\overline{\delta_u}$,n) and the bubble layer (k_δ, $g(\eta)$) for a given hydrofoil to that found in the flat plate, the impact of local changes in the void fraction on the $\Delta(DR)_3$ term would be enhanced on the suction face. Moreover, this enhacement would be greater the higher the angle of attack of the airfoil. For example, considering the case of a NACA 0012 hydrofoil at an angle of attack of 10°, the viscous stress reduction term $\Delta(DR)_3$ would be enhanced by a factor of 6 at the point of maximum suction when compared to that of the flat plate (An et al., 2022). On the other hand, at the pressure face the contribution of $\Delta(DR)_3$ in Eq. (37) would be smaller than in the flat plate case. Therefore, according to Eq. (43), it will be especially relevant to avoid a decrease of the wall void fraction at the suction face.

4.3. Contribution of the void fraction to the drag reduction

The contribution of the void fraction to the drag reduction is the sum of the first two terms on the right hand in Eq. (37). The second term appears as a consequence of the existence of a pressure gradient and has already been discussed in a previous subsection. Therefore, the first term is going to be discussed in this subsection. This contribution can be expressed as follows:

$$\Delta(DR)_1 = g_0 g_1 \overline{U_e}^2 \alpha_w = \frac{2C_1}{c_{f0}} g_1 (1-c_p)\alpha_w \tag{44}$$

Where

$$g_1 = \left(\overline{\delta_u}\frac{dH_1}{d\zeta} + H_1\frac{d\overline{\delta_u}}{d\zeta}\right) \tag{45}$$

Given the existence of a term of form $(1-c_p)$ in Eq. (44), similar conclusions can be drawn as discussed for Eq. (43), with the exception that the g_1 term defined in Eq. (45) introduces the possibility that $\Delta(DR)_1 < 0$. Thus, in order to obtain a drag reduction by this term, it is necessary that $\Delta(DR)_1 > 0$. The sign of C_1, c_{f0}, $(1-c_p)$ and α_w are always positive. Therefore, the sign of g_1 should be positive to reduce drag by this term. Moreover, the sign of $\overline{\delta_u}$ and H_1 are also positive.

Regarding the term $\frac{dH_1}{d\zeta}$, it can be calculated from Eq. (32) as follows:

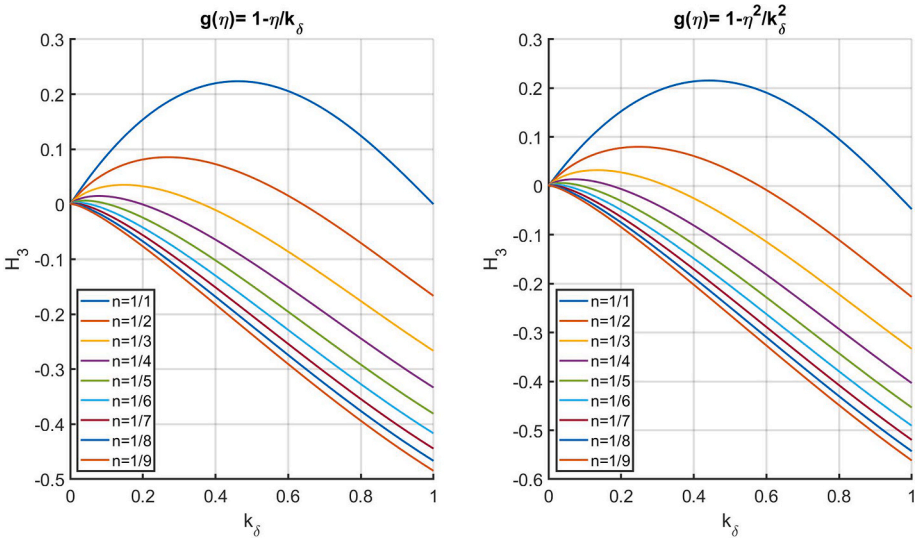


Fig. 7. Function H_3 for linear and quadratic density functions.

$$\frac{dH_1}{d\zeta} = k_\delta^n(1-k_\delta^n)\frac{dk_\delta}{d\zeta} = H_4\frac{dk_\delta}{d\zeta} \tag{46}$$

The value of H_4 as a function of k_δ for different boundary layers exponent values is plotted in Fig. 8 where it can be observed the existence of a maximum of value 0.25 for all curves. Since k_δ is less or equal to the unity under the proposed assumptions, H_4 is always positive and the sign of $\frac{dH_1}{d\zeta}$ is the same as $\frac{dk_\delta}{d\zeta}$. Therefore, it is convenient that $\frac{dk_\delta}{d\zeta} > 0$ so that this term contributes to reduce drag. This suggests that in order to reduce viscous stresses, it is always advantageous for the bubble layer to grow at a faster rate than the boundary layer. Note that in the cases where $\frac{dk_\delta}{d\zeta} = 0$, then $\frac{dH_1}{d\zeta} = 0$ and therefore $g_1 = H_1\frac{d\overline{\delta_u}}{d\zeta}$.

Nevertheless, for a given boundary layer and a given value of k_δ, it is possible to define a negative critical gradient $\frac{dk_\delta}{d\zeta}_{crit}$ above which the term g_1 is still positive. If considering the case of the Prandtl boundary layer ($n = 1/7$), whose boundary layer thickness can be defined through the semi-empirical equation $\overline{\delta_u} = 0.16Re_c^{-1/7}\zeta^{6/7}$, (being Re_c the Reynolds number where the characteristic length is the chord), it is possible to compute the critical gradient $\frac{dk_\delta}{d\zeta}_{crit}$ for different values of k_δ. The results are represented in Fig. 9 for values of k_δ between 0.2 and 0.8. It can be inferred from the figure that smaller thicknesses of the bubble layer k_δ exhibit a smaller value of the critical gradient $\frac{dk_\delta}{d\zeta}_{crit}$ so that it is more likely that the local decrease of k_δ (that will occur if $\frac{dk_\delta}{d\zeta} < 0$) could result in $\Delta(DR)_1 < 0$. In the limit case when $k_\delta \to 0$, it is found that any decreasing value in k_δ generates a negative contribution in drag reduction, $\frac{dk_\delta}{d\zeta}_{crit} \to 0$. In the opposite case when $k_\delta \to 1$, it is found that the limit $\frac{dk_\delta}{d\zeta}_{crit} \to -\infty$.

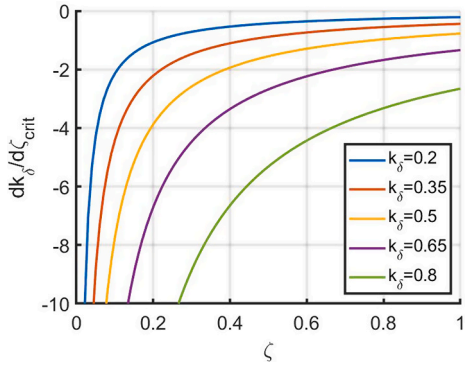


Fig. 9. Limit values of the gradient $\frac{dk_\delta}{d\zeta}_{crit}$ for different values of k_δ below which $\Delta(DR)_1 < 0$

Another case of interest might be the one in which the physical thickness of the bubble layer δ_ρ remains practically unchanged so that it can be considered as constant. Under these conditions the expression g_1 would be negative for $k_\delta > H_1/H_4$ (considering $\frac{d\overline{\delta_u}}{d\zeta} > 0$). Such case is

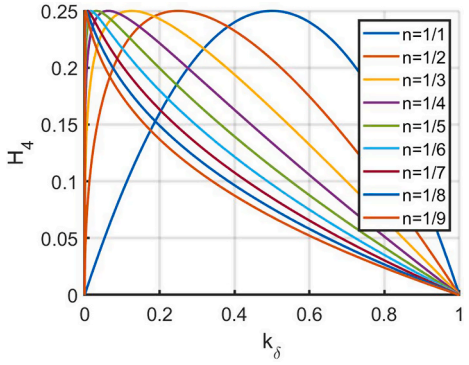


Fig. 8. Function H_4 as a function of k_δ for different n exponent values.

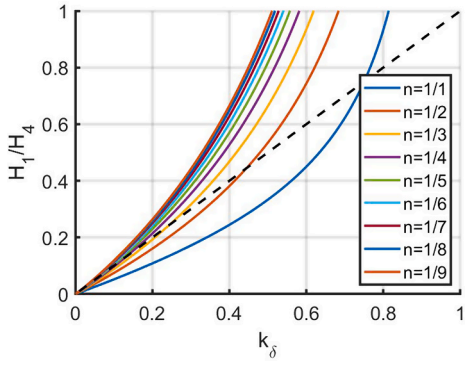


Fig. 10. Values of k_δ for different n exponent values for a constant bubble layer thickness case where $g_1 < 0$ (above the dash line) and $g_1 > 0$ (below the dash line).

illustrated in Fig. 10 for different values of the exponent n. The diagonal dividing line separating the regions where $g_1 < 0$ (above the line) and $g_1 > 0$ (below the line) is depicted for illustrative purposes. Thus, for example, for $n = 1/7$, values of $k_\delta > 0.017$ will always make $\Delta(DR)_1$ contribute positively to the drag reduction.

Finally, it is important to point out that, as compared with previous models for flat plates (i.e Park et al., 2016), in this model instead of an average void fraction, the distribution of bubbles has been characterized by the proportion of the thickness of the region with bubbles in the boundary layer k_δ and void fraction at the wall α_w, which could be magnitudes easier measured experimentally. Therefore, it is expected that the decoupling of the effects of bubble region growth from those corresponding to the bubble presence close to the wall may exhibit benefits from an experimental and numerical point of view. Nevertheless, the average void fraction defined by Park et al. (2016) could be calculated from the variables proposed in here as follows:

$$\alpha_\delta = k_\delta \alpha_w \int_0^1 g(\xi) d\xi \tag{47}$$

5. Conclusions

The drag reduction phenomena in hydrodynamic profiles as a consequence of the presence of microbubbles in their boundary layer has been studied from a theoretical point of view. For this purpose, a model based on a compressible von Karman integral equation has been proposed, where the density has been modeled as a scalar quantity that behaves in a self-similar way in a direction tangential to its surface. As a result, it has been possible to express the drag reduction as the sum of three terms related to the pressure gradient, the wall void fraction and the local wall void fraction gradient. Given the definition of drag reduction, the terms will contribute to reduce the drag when they are greater than zero.

Based on a theoretical analysis, it has been concluded that the term related to the pressure gradient shows a performance change with the possibility of a negative or positive contribution depending on the boundary layer structure, the distribution of the void fraction within the bubble layer and the relative thickness between the two layers. In order to qualitatively evaluate the expected behavior for given boundary layers, a sign map has been represented which, using a bubble distribution function, allows to determine the regions where the presence of bubbles in the presence of a pressure gradient will contribute positively to the local drag reduction. In relation to the term linked to the wall void fraction gradient, it shows the expected behavior, similar to the flat plate case, where its contribution to the drag reduction will be positive whenever the void fraction in the wall increases, contributing negatively when it decreases. On the other hand, it has been determined that for a given boundary layer and bubble layer, the effect of the local void fraction on viscous stress reduction increases the lower the value of the local pressure coefficient. It is therefore particularly relevant to realize the necessary contribution of bubbles on the suction side, in particular for high angles of attack. This effect of increasing the local pressure coefficient has been also noted for the wall void fraction term with the main difference that there is the possibility of a negative contribution in situations where the boundary layer grows at a much higher rate than the bubble layer.

Summarizing, the drag reduction in an airfoil due to the presence of microbubble inside the boundary layer can be divided into three terms related to either the pressure gradient, the void fraction or the void fraction gradient. From the theoretical research conducted for each of these terms, it has been concluded that in order to make the pressure gradient beneficial to the drag reduction, as long as there is enough void fraction inside the boundary layer, the bubbles should be present in those region where there is positive pressure gradient and the void fraction should increase along the chord. On the contrary, if there were not enough void fraction, the bubbles would be beneficial to drag reduction in the regions where there is a negative pressure gradient. Nevertheless, all the conclusions draught in this study depart from theoretical assumptions and experimental results are needed to confirm these conclusions.

CRediT authorship contribution statement

Adelaida García-Magariño: Writing – review & editing, Writing – original draft, Validation, Software, Methodology, Investigation, Formal analysis, Conceptualization. **Suthyvann Sor:** Writing – review & editing, Writing – original draft, Validation, Software, Methodology, Investigation, Formal analysis, Conceptualization. **Rafael Bardera:** Writing – review & editing, Writing – original draft, Validation, Software, Methodology, Investigation, Formal analysis, Conceptualization. **Pablo López-Gavilán:** Writing – review & editing, Writing – original draft, Validation, Software, Methodology, Investigation, Formal analysis, Conceptualization.

Declaration of competing interest

The authors declare that they have no known competing financial interests or personal relationships that could have appeared to influence the work reported in this paper.

Acknowledgments

This research was funded by the INTA internal project BIFLOWPROP with internal code S.IGB22001. This study has been funded by the Spanish Ministry of Science, Innovation and University under the research contract PID2023-152827NA-I00 by the project HYDRO-BUBBLE entitled “Reduccion de esfuerzos viscosos mediante flujos bifasicos en la capa limite aplicables a la propulsion marina”. The author want to thank to all the personnel at INTA-CEHIPAR for his support during this research.

Appendix A

In this section, the dynamic equations of an isolated bubble are discussed more extensively in order to evaluate the forces that most significantly impact the growth of the bubble layer, assessing the validity of the assumptions that support the periodic axisymmetric flow and a plane domain in the framework of the proposed model. It must be emphasised that the following discussion aims to analyse the relative significance of the different forces related to the motion of an isolated bubble without attempting to characterize the distribution of the bubble layer.

Based on the work of Gabillet et al. (2002), the equation of motion of an isolated spherical particle of diameter d_b can be expressed in local Cartesian coordinates with velocity $\vec{u}_b = (u_b, v_b, w_b)$ being respectively the tangential, normal and transverse velocity to the plane domain. Since the density of the gas phase is much lower than that of the liquid phase, it is possible to neglect the inertia of the bubble. On the other hand, it is possible to express the drag coefficient in the form $C_D = k/Re_b$ being k itself a function of Re_b, which based on experimental results on bubbles with bubble Reynolds numbers $Re_b < 10^2$ can be expressed as $k = 17\, Re_b$, so that $C_D = 17/Re_b^{-2/3}$. The equations of motion of the bubble in the tangential and normal direction will be respectively:

$$C_A\frac{du_b}{dt} = -\frac{3k}{4}\frac{\nu_L}{d_b^2}(U_L - u_b) + C_L v_b\frac{dU_L}{dy} \tag{A.1}$$

$$C_A\frac{dv_b}{dt} = -\frac{3k}{4}\frac{\nu_L}{d_b^2}v_b + g + C_L(U_L - u_b)\frac{dU_L}{dy} \tag{A.2}$$

where C_A and C_L are the added mass and lift coefficients respectively (which standard value for the sphere is 0.5), ν_L the kinematic viscosity of the liquid phase and U_L the free stream velocity (as seen by the bubbles inside the boundary layer). When the bubble moves at the stream velocity, so that the relative velocity $(U_L - u_b) = 0$, it is possible to estimate the terminal vertical velocity of the bubble as:

$$v_b = 0.15 g^{3/4} d_b^{5/4}\,\nu_L^{-1/2} \tag{A.3}$$

It is of interest to analyse the time necessary for the bubble to reach a vertical distance equivalent to that of the boundary layer. Considering in a first rough estimation the case of a turbulent boundary layer developed over a flat plate, its thickness takes the following semiempirical expression:

$$\delta_u = 0.16\; c\; Re^{-\frac{1}{7}} \tag{A.4}$$

It is possible to estimate the time it takes for the bubble to leave the boundary layer using equations A.3 and A.4:

$$t_b = \frac{\delta_u}{v_b} \sim c\, Re^{-\frac{1}{7}} g^{-3/4} d_b^{-5/4}\,\nu_L^{1/2} \tag{A.5}$$

The velocity w_b is included given that in the case under study there is a centrifugal force on the bubble caused by the rotating reference frame. This centrifugal force can be expressed as follows:

$$F_C = \frac{\pi}{6}\, d_b^3\, \rho_g\;\; \omega^2\, R = \rho_g\frac{\pi}{6}\;\; d_b^3\frac{V_\theta^2}{R} \tag{A.6}$$

where R is the distance to the rotation axis of the blade section under consideration and ω is the rotation speed. In this case, the equilibrium equation in traverse direction would be:

$$C_A\frac{dw_b}{dt} = -\frac{3k}{4}\frac{\nu_L}{d_b^2}w_b + \frac{\rho_g}{\rho_l}\;\frac{V_\theta^2}{R} \tag{A.7}$$

Defining the density ratio as $\overline{\rho} = \rho_g/\rho_L$ and considering that forces are at equilibrium and substituting the hydrodynamic drag coefficient expression, the transverse terminal velocity would be:

$$w_b = 0.15\overline{\rho}^{3/4}\; V_\theta^{3/2} R^{-3/4} d_b^{5/4}\;\nu_L^{-1/2} \tag{A.8}$$

In a conservative analysis, we can approximate $V_\theta \sim U_\infty$ (since we know that $V_\theta < U_\infty$), which allow to express the ratio as a function of the Reynolds number for a blade element ($Re\;(r = R)$) as:

$$w_b = 0.15\overline{\rho}^{3/4} c^{-3/2}\; Re^{3/2}\; R^{-3/4} d_b^{5/4}\;\nu_L \tag{A.9}$$

Proceeding in analogy to equation (A.5) for the vertical velocity, the time it takes for a bubble to travel a transverse distance equal to the boundary layer thickness can be expressed as:

$$t_c = \delta_u/w_b \sim \overline{\rho}^{-3/4} R^{3/4} d_b^{-5/4}\;\nu_L^{-1} Re^{-\frac{19}{14}} c^{5/2} \tag{A.10}$$

It is of interest to compare these characteristic times with the residence time of the bubble along the blade section:

$$t_r \sim c^2 Re^{-1}\nu_L^{-1} \tag{A.11}$$

The comparison between the residence time (Eq. (A.11) and the characteristic times described in Equation (A.5) and Equation (A.10) show the relative importance of the gravitational and centrifugal forces in the particle motion and assess the axisymmetric and plane problem assumptions. Specifically, under the conditions $\Pi_b = t_r/t_b \ll 1$ and $\Pi_c = t_r/t_c \ll 1$ the proposed model would be reasonably applicable for the considered blade cross-section operating under a given flow and rotating speed. The balance will therefore be:

$$\Pi_b = \frac{t_r}{t_b} \sim\;\; cRe^{-6/7}\nu_L^{-3/2} g^{3/4} d_b^{5/4} \tag{A.14}$$

$$\Pi_c = \frac{t_r}{t_c} \sim \overline{\rho}^{3/4}\; Re^{5/14} c^{-1/2}\; R^{-3/4} d_b^{5/4} \tag{A.15}$$

These balances are plotted below (Fig. A1 and Fig. A2) for the case of micrometresized bubbles ($1\;\mu m < d_b < 100\;\mu m$) and Reynolds numbers between $0.5{\cdot}10^6 < Re < 10^8$, for a blade element with chord, $c = 1\;m$, at $R = 3\;m$ from the rotating axis, being $g = 9.8\;m/s^2$, $\nu_L = 8.9{\cdot}10^{-7}\;m^2/s$ and density ratio $\overline{\rho} = 1.2{\cdot}10^{-3}$.

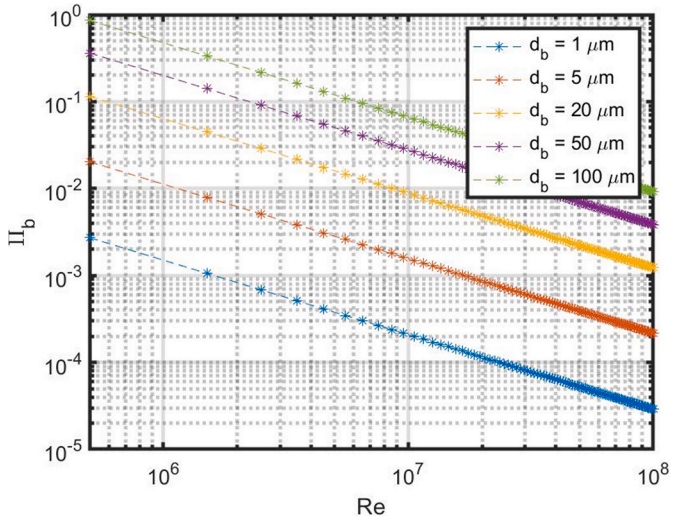


Fig. A1. Importance of buoyancy effect.

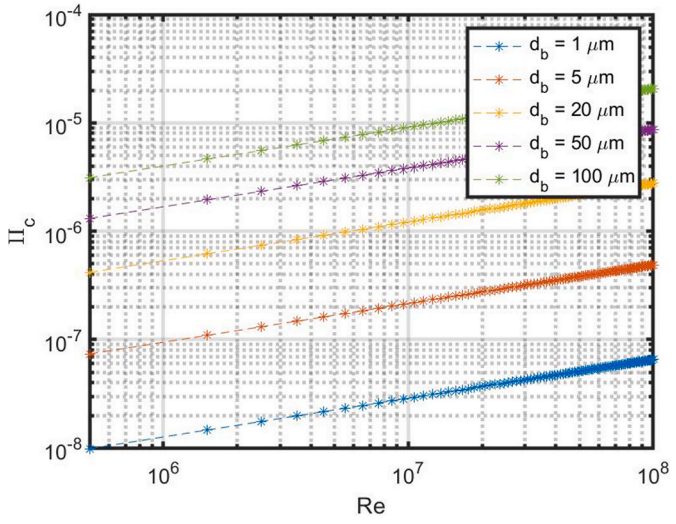


Fig. A2. Importance of centrifugal effect.

References

An, H., Pan, H., Yang, P., 2022. Research Progress of air lubrication drag reduction technology for ships. Fluids 7 (10), 319.

Bae, H.S., Kim, W.K., Son, S.U., Park, J.S., 2022. Imaging of Artificial bubble distribution using a Multi-Sonar Array system. J. Mar. Sci. Eng. 10 (12), 1822.

Benini, E., 2004. Significance of blade element theory in performance prediction of marine propellers. Ocean Eng. 31 (8–9), 957–974.

Ceccio, S.L., 2010. Friction drag reduction of external flows with bubble and gas injection. Annu. Rev. Fluid Mech. 42 (1), 183–203.

Elbing, B.R., Winkel, E.S., Lay, K.A., Ceccio, S.L., Dowling, D.R., Perlin, M., 2008. Bubble-induced skin-friction drag reduction and the abrupt transition to air-layer drag reduction. J. Fluid Mech. 612, 201–236.

European Maritime Transport Environmental Report, 2021. Available online:. https://www.eea.europa.eu/publications/maritime-transport. (Accessed 13 December 2023).

Feng, Y.Y., Hu, H., Peng, G.Y., Zhou, Y., 2020. Microbubble effect on friction drag reduction in a turbulent boundary layer. Ocean Eng. 211, 107583.

Gabillet, C., Colin, C., Fabre, J., 2002. Experimental study of bubble injection in a turbulent boundary layer. Int. J. Multiphas. Flow 28 (4), 553–578.

Gao, F., Bloch, F., Brodtkorb, A.H., 2023. Novel combinator surface concept for efficiency optimization of ship propulsion system. Ocean Eng. 280, 114489.

García-Magariño, A., Lopez-Gavilan, P., Sor, S., Terroba, F., 2023. Micro/Bubble drag reduction focused on new applications. J. Mar. Sci. Eng. 11 (7), 1315.

Guin, M.M., Kato, H., Yamaguchi, H., Maeda, M., Miyanaga, M., 1996. Reduction of skin friction by microbubbles and its relation with near-wall bubble concentration in a channel. J. Mar. Sci. Technol. 1, 241–254.

Hufford, G.S., Drela, M., Kerwin, J.E., 1994. Viscous flow around marine propellers using boundary-layer strip theory. J. Ship Res. 38 (1), 52–62.

Jessup, S.D., 1989. An Experimental Investigation of Viscous Aspects of Propeller Blade Flow. The Catholic University of America.

Kawamura, T., Ito, A., Hinatsu, M., 2007. Numerical simulation of bubbly flow around a marine propeller. FEDSM 42894, 449–454.

Kim, S.H., Roh, M.I., Oh, M.J., Park, S.W., Kim, I.I., 2020. Estimation of ship operational efficiency from AIS data using big data technology. Int. J. Nav. Archit. Ocean Eng. 12, 440–454.

Kim, Y.R., Steen, S., 2023. Potential energy savings of air lubrication technology on merchant ships. Int. J. Nav. Archit. Ocean Eng. 15, 100530.

Kumar, S., Pandey, K.M., Sharma, K.K., 2021. Advances in drag-reduction methods related with boundary layer control–A review. Mater. Today Proc. 45, 6694–6701.

Leal, L.G., 2007. Advanced Transport Phenomena: Fluid Mechanics and Convective Transport Processes, vol. 7. Cambridge university press.

Lee, J.H., Park, H.G., Kim, J.H., Lee, K.J., Seo, J.S., 2014. Reduction of propeller cavitation induced hull exciting pressure by a reflected wave from air-bubble layer. Ocean Eng. 77, 23–32.

Li, Q.Y., Yongpeng, O., 2012. A numerical study of the effect of bubble layer on propulsion performance of deep-vee hull form ship. Adv. Mater. Res. 479, 2551–2556.

Li, J., Martin, J.E., Carrica, P.M., 2019. Large-scale simulation of ship bubbly wake during a maneuver in stratified flow. Ocean Eng. 173, 643–658.

Mattson, M., Mahesh, K., 2011. Simulation of bubble migration in a turbulent boundary layer. Phys. Fluids 23 (4).

Mawignon, F.J., Liu, J., Qin, L., Kouediatouka, A.N., Ma, Z., Lv, B., Dong, G., 2023. The optimization of biomimetic sharkskin riblet for the adaptation of drag reduction. Ocean Eng. 275, 114135.

Mørch, K.A., 2009. Cavitation nuclei: experiments and theory. J. Hydrodyn. 21 (2), 176–189.
Murai, Y., 2014. Frictional drag reduction by bubble injection. Exp. Fluid 55, 1–28.
Nadery, A., Ghassemi, H., Chybowski, L., 2021. The effect of the PSS configuration on the hydrodynamic performance of the KP505 propeller behind the KCS. Ocean Eng. 234, 109310.
Nuchturee, C., Li, T., Xia, H., 2020. Energy efficiency of integrated electric propulsion for ships–A review. Renew. Sustain. Energy Rev. 134, 110145.
Park, H.J., Hamada, T., Kawakita, C., Murai, Y., 2023. Vertical diffusion of bubbles injected beneath a flat-bottomed ship for frictional drag reduction. Ocean Eng. 289, 116248.
Park, H.J., Oishi, Y., Tasaka, Y., Murai, Y., 2016. Void waves propagating in the bubbly two-phase turbulent boundary layer beneath a flat-bottom model ship during drag reduction. Exp. Fluid 57, 1–18.
Reisman, G.E., Duttweiler, M.E., Brennen, C.E., 1997. Effect of air injection on the cloud cavitation of a hydrofoil. AME Fluids Engineering Division Summer Meeting FEDSM9–3249.
Ren, H., Ding, Y., Sui, C., 2019. Influence of EEDI (energy efficiency design Index) on ship–engine–propeller matching. J. Mar. Sci. Eng. 7 (12), 425.
Sanders, W.C., Winkel, E.S., Dowling, D.R., Perlin, M., Ceccio, S.L., 2006. Bubble friction drag reduction in a high-Reynolds-number flat-plate turbulent boundary layer. J. Fluid Mech. 552, 353–380.
Simonsen, M., Walnum, H.J., Gössling, S., 2018. Model for estimation of fuel consumption of cruise ships. Energies 11 (5), 1059.
Sindagi, S., Vijayakumar, R., 2021. Succinct review of MBDR/BDR technique in reducing ship's drag. Ships Offshore Struct. 16 (9), 968–979.
Tadros, M., Ventura, M., Guedes Soares, C., 2021a. Design of propeller series optimizing fuel consumption and propeller efficiency. J. Mar. Sci. Eng. 9 (11), 1226.
Tadros, M., Vettor, R., Ventura, M., Guedes Soares, C., 2021b. Coupled engine-propeller selection procedure to minimize fuel consumption at a specified speed. J. Mar. Sci. Eng. 9 (1), 59.
Tadros, M., Ventura, M., Guedes Soares, C., 2022a. Towards fuel consumption reduction based on the optimum contra-rotating propeller. J. Mar. Sci. Eng. 10 (11), 1657.
Tadros, M., Vettor, R., Ventura, M., Guedes Soares, C., 2022b. Effect of propeller cup on the reduction of fuel consumption in realistic weather conditions. J. Mar. Sci. Eng. 10 (8), 1039.
Tadros, M., Ventura, M., Guedes Soares, C., 2023. Effect of hull and propeller roughness during the assessment of ship fuel consumption. J. Mar. Sci. Eng. 11 (4), 784.
Vahaji, S., Chen, L., Cheung, S.C., Tu, J., 2018. Numerical investigation on bubble size distribution around an underwater vehicle. Appl. Ocean Res. 78, 254–266.
Vakarelski, I.U., Kamoliddinov, F., Jetly, A., Thoroddsen, S.T., 2021. When superhydrophobicity can be a drag: Ventilated cavitation and splashing effects in hydrofoil and speed-boat models tests. Colloids Surf. A Physicochem. Eng. Asp. 628, 127344.
Wang, C., Huang, B., Zhang, M., Wang, G., Wu, Q., Kong, D., 2018. Effects of air injection on the characteristics of unsteady sheet/cloud cavitation shedding in the convergent-divergent channel. Int. J. Multiphas. Flow 106, 1–20.
Wang, H., Wang, K., Liu, G., 2022. Drag reduction by gas lubrication with bubbles. Ocean Eng. 258, 111833.
Wu, T.S., Kinnas, S.A., 2025. Propeller performance prediction via 3D coupling of BEM with boundary layer solver. Ocean Eng. 321, 120396.
Wu, H., Ou, Y., Ye, Q., 2020. Numerical study on the influence of air layer for propeller performance of large ships. Ocean Eng. 195, 106681.
Xia, W., Song, W., Wang, C., Yi, W., Meng, Q., Deng, H., 2023. Microbubbles drag reduction characteristics of underwater vehicle during pitching movement. Ocean Eng. 285, 115350.
Xing, H., Spence, S., Chen, H., 2020. A comprehensive review on countermeasures for CO2 emissions from ships. Renew. Sustain. Energy Rev. 134, 110222.
Yin, C., Rosenvinge, C.K., Sandland, M.P., Ehlers, A., Shin, K.W., 2023. Improve ship propeller efficiency via optimum design of propeller boss cap Fins. Energies 16 (3), 1247.
Yu-Zhe, F., Bao-Wei, C., Hai-Sen, L., Chao, X., 2018. Linear-wave propagation in liquids containing bubbly clusters. Acta. Phys. Sin. 67 (17).
Zhang, X., Wang, J., Wan, D., 2020. Euler–Lagrange study of bubble drag reduction in turbulent channel flow and boundary layer flow. Phys. Fluids 32 (2).
Zhao, X., Zong, Z., 2022. Experimental and numerical studies on the air-injection drag reduction of the ship model. Ocean Eng. 251, 111032.
Zhen, T., Liu, J., Qin, L., Lu, S., Mawignon, F.J., Ma, M., Hao, L., Wu, Y., An, D., Dong, G., 2024. Effect of dolphin-inspired transverse wave microgrooves on drag reduction in turbulence. Phys. Fluids 6, 015157.